

Study of a Diagnostic Technique for Nasal Obstruction Evaluation

Maria Beatriz da Rocha Marques
beatriz.marques@tecnico.ulisboa.pt

Instituto Superior Técnico, Lisboa, Portugal

November 2018

Abstract

Nasal obstruction is the main symptom of many nose related diseases and one of the most common causes of medical visits. It has a strong impact on the quality of life of patients of every age. The characterization of this condition is important for the correct identification of its cause. The objective diagnostic tools that are available present some problems and there is a lack of simple, noninvasive and cost-effective procedures. This thesis presents a step towards a technique for nasal obstruction assessment that aims to answer this need. In this technique, the measurement of the nostril expiratory velocity is performed using a microphone and a cylinder-shaped barrier, taking advantage of the vortex shedding phenomenon. An experimental study to evaluate this technique was performed, mainly to verify the existence of vortex shedding and determine operating parameters by attempting to measure the vortex shedding frequency. The tests were executed for different barriers, with diameters (D) of 1 mm, 2 mm and 5 mm. The visualization of the vortex shedding was achieved for $D=5$ mm, better accomplished in the near wake region. The vortex shedding frequency was successfully obtained for $D=2$ mm and flow velocities ranging from 1.40 m/s to 2.10 m/s, with a Strouhal number of 0.2 that shows agreement with literature. Additionally, an optimal position for the microphone was determined for this diameter. This work accomplishes a first step in the study of this technique, which aims to be a simple and straightforward way to test nasal patency.

Keywords: nasal obstruction, vortex shedding, diagnostic technique, nostril expiratory velocity

1. Introduction

Nasal obstruction is one of the main symptoms, not a diagnosis, of various conditions that affect the nose [1]. It is defined as the sensation of insufficient airflow passing through the nasal airways. Its principal cause is the deviated septum condition, that affects up to 80% of people [2].

Overall, it is estimated that about one-third of the population has some kind of nasal obstruction, from which one-quarter seeks surgical treatment [3]. Considering the high number of people that suffer from this problem, its study is important, in particular the developing of diagnostic techniques.

When performing a diagnosis, the first step involves the evaluation of the patient's symptoms. In nose related diseases, this includes nasal obstruction assessment. This evaluation can be performed using subjective diagnostic tools, as symptom scores and visual analogue scales, or objective ones [4], which are often preferable for being quantitative.

Although already very developed, the objective diagnostic tools present some problems related to the difficulty in quantifying this condition [5]. This

occurs mainly due to the highly complex structure of the nasal cavity, that possesses intricate and narrow channels essential to fulfill its functions. The nasal cavity heats and humidifies the inhaled air while removing noxious materials. It also permits olfaction, since it has receptors for the sense of smell [6].

An additional reason for the difficulty in quantifying nasal obstruction is the nasal cavity's significant intra and inter-subject differences. For example, the adaptation to climate led to differences in nasal morphology between subjects of differing origins [7]. Besides this, there is also an intra-individual variation between the left and right side of the nasal cavity, caused by the nasal cycle [8].

Currently, the most used objective diagnostic techniques are anterior rhinomanometry, peak nasal inspiratory flow and acoustic rhinometry [9]. In general, these procedures have some problems, for instance, the dependence on the patient's effort, the need for skilled technicians and the fact that the test is expensive, invasive and slow [10, 11].

An ideal test to evaluate nasal obstruction that

is simple, noninvasive and cost-effective would represent an improvement on the life of many people that suffer from this condition. This work represents an attempt to develop a technique to answer this need.

The proposed technique has the goal of determining the expiratory velocity near each nostril using the vortex shedding phenomenon. Accordingly, the particular focus of this work is to assess if this is feasible. With this objective, a personalized experimental setup was built, where a series of tests were carried to evaluate and define specific parameters for the technique's operation.

The goal of building an experimental setup, instead of testing directly on human nostrils, is to have more control over the performed experiments. The human nose is highly complex, as it is the nostril expiratory velocity profile. By designing a setup, some of this complexity is removed, and the performed study becomes easier to execute.

The relation between the expiratory velocity at each nostril and the evaluation of nasal obstruction is not yet investigated. Along with the analysis of this technique, further studies need to be done to understand this relation. However, in the clinical environment quantitative measurements are always needed, which is exactly what this technique purposes. When pondering about the future of healthcare, one important aspect is the change from a curative system to a more preventive one [12]. To accomplish this, it is expected that simple techniques like this one will have an important role.

2. Background

2.1. Vortex Shedding

The vortex shedding is an oscillating flow that occurs for certain Reynolds numbers (Re) when a fluid finds a bluff body, depending on the size and shape of the same. As the flow passes a bluff body, it is split into two streams and the instability of the shear layer causes the formation of vortices that are shed alternately from each side. The frequency of these vortices (f_v) is a function of the flow velocity (V) and the characteristic length of the body (L) [13]. This relation is presented by the Strouhal number (St), defined as:

$$St = \frac{f_v L}{V}. \quad (1)$$

Cylinders with a circular cross-section are a traditional example of a bluff body and the better documented one [14]. For this geometry, the flow's dependence on the Reynolds number is known, and it is reported the beginning of a vortex street for $Re \geq 49$ [15].

The Strouhal number can be represented as a function of the Reynolds number. In Figure 1, this dependence is shown for the case of a cylinder. It

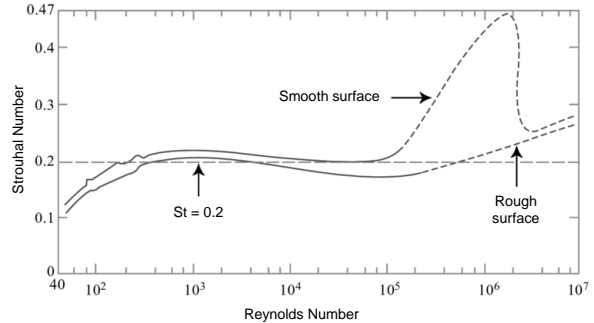


Fig. 1: Strouhal number as a function of the Reynolds number (adapted from [16]).

can be observed that the Strouhal number is around 0.2 for a large Reynolds number interval. This fact is important since it enables the estimation of the flow velocity by measuring the released vortices.

2.2. Operation Principle

The proposed technique has the aim of measuring the expiratory flow velocity for both nostrils separately, enabling further comparisons. In order to do this, a cylinder-shaped barrier is placed near the nostril. When expiring, the air encounters the barrier that releases vortices at a specific frequency. Then, a microphone placed after the cylinder captures the pressure fluctuations caused by the vortices. A simple schematic view of this arrangement is portrayed in Figure 2.

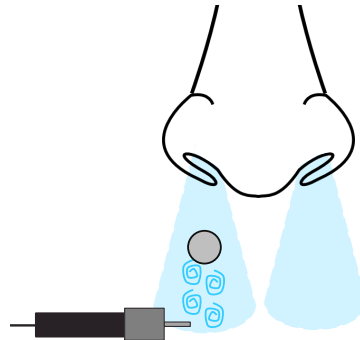


Fig. 2: Scheme of the proposed technique.

After the acquisition of the pressure fluctuations by the microphone, a signal processing system determines the vortex shedding frequency. Then, the expiratory flow velocity can be calculated using the Strouhal number equation:

$$St = \frac{f_v L}{V} \Rightarrow V = \frac{f_v L}{St}, \quad (2)$$

where f_v is the captured frequency and L is the diameter of the cylinder. Regarding St_t , the value used should be an estimation of its real value for the ana-

lyzed case, so that the estimation of the expiratory velocity is accomplished. At first sight, and taking into consideration Figure 1, the most probable value is $St = 0.2$. However, further investigation needs to be done to verify its application in this case.

In order to guarantee the correct measurement of the expiratory velocity, some aspects of this technique are analyzed. Firstly, it is verified the presence of vortex shedding in the analyzed case, using the experimental setup presented in the next section. Then, in the same setup, it is measured the vortex shedding frequency. With the gathered results, the Strouhal number is estimated, along with the determination of the optimal barrier diameter. Furthermore, the optimal positions of the barrier and the microphone are determined.

3. Experiment

3.1. Setup

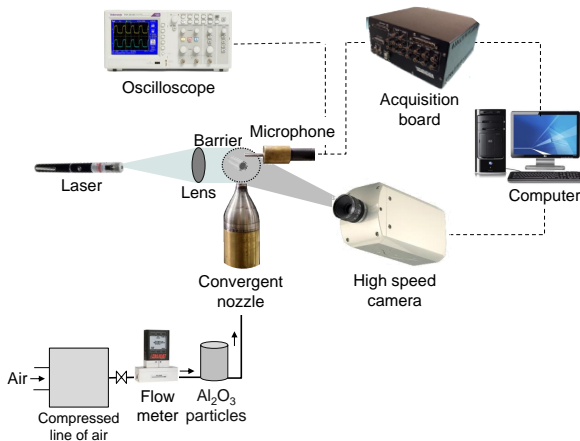


Fig. 3: Experimental setup scheme.

A global illustration of the experimental setup is presented in Figure 3. It is constituted by a convergent nozzle connected to a flow meter that controls the input of air. The flow meter is from 16 Series Alicat Scientific and has a maximum capacity of 20 standard liters per meter (SLPM). A maximum uncertainty ± 0.14 SLPM was registered.

The convergent nozzle has a circular outlet with a diameter of 11 mm and an area contraction ratio of 13.22. This geometry leads to a stationary, laminar and plug flow at the exit. Additionally, it has an outlet area of 0.950 cm^2 . Although the nostril area is quite variable between subjects, some studies already estimated it to be $\sim 1 \text{ cm}^2$ [17]. This is important since it allows a resemblance with the human nose.

As it can be observed in Figure 4, near the flow outlet there is a barrier responsible for the formation of the desired vortices, and a microphone that measures the pressure fluctuations caused by them. In this setup, the position of the microphone and

barrier related to the flow outlet was adjustable with millimeter accuracy due to the presence of a macro rail support system.

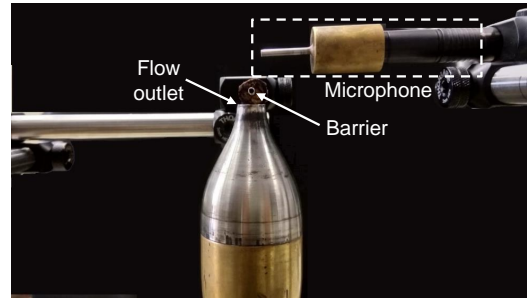


Fig. 4: Real experimental conditions.

In the performed experiments, three distinct cylinder-shaped barriers were used with the diameters (D) of 5 mm, 2 mm and 1 mm.

The microphone was utilized together with an acoustic probe. The microphone is from Brüel & Kjær type 4189, with a linear response in the range of 6.3 Hz to 10 kHz. Regarding the acoustic probe, it has a tube with an inner diameter of 3 mm and a length of 20 mm. These dimensions enabled a linear frequency response up to 600 Hz, which is appropriate for the performed experiments. The choice to use an acoustic probe has to do with the need for a smaller diameter device for acquiring the desired measurements.

The pressure fluctuations detected through the microphone were acquired by the Data Translation DT9841-VIB-SB board. Each run of acquisition was composed of $N=50$ blocks of 20,000 points, acquired at a sampling frequency $f_s=10 \text{ kHz}$, resulting in a frequency resolution of 0.5 Hz. This produced an output file of 1 million points that was post-processed in MATLAB[®], where the response in the frequency domain was investigated using the Fast Fourier Transform (FFT).

Besides this, a high-speed camera is pointed to the flow outlet, to verify the existence of vortex shedding. The camera is a high-speed CCD video camera Phantom v4.2. It permits a sampling rate up to 2200 frames per second (fps) with a maximum resolution of 512×512 pixels.

A planar visualization for recording is provided by the laser, lens, mirror and the added aluminum oxide particles. The camera is connected to the computer to allow processing the acquired frames.

The oscilloscope Tektronix tds 2012c was mostly used at the beginning of the experimental work. It was helpful in verifying the correct operation of the acquisition board, microphone and the developed code.

3.2. Procedure

For convenience reasons, the experimental tests were divided into two parts. The high speed imaging system, that aims to verify the existence and record the vortex shedding phenomenon, and the pressure detection system, which has the objective of obtaining the vortex shedding frequency.

In the case of the high speed imaging system, the air flow rate was varied between 1 SLPM and 12 SLPM. Along with this, some parameters of the high-speed camera were changed. The fps was varied between 400 fps and 2200 fps, in which the resolution and exposure time were set to the maximum.

In addition, the diameter of the barrier was varied, along with its position related to flow outlet. After some tests, the parameters that provided for better visualization were defined: a barrier of 5 mm set to a distance of D from the outlet.

For the pressure detection system, the air flow rate was varied between 4 SLPM and 12 SLPM. The initial objective was to choose values that imposed an outlet velocity around 1 m/s, according to the study [18] that measured expiratory nasal velocities. However, for a flow rate smaller than 4 SLPM, the pressure detection system almost did not detect the pressure fluctuations. Taking this into account, the values chosen are presented in Table 1.

Table 1: Flow rate and respective outlet velocity.

Q [SLPM]	V [m/s]
4	0.70
6	1.05
8	1.40
10	1.75
12	2.10

Besides the flow rate variation, the three different barriers were used. Its position was also kept at a distance of D from the outlet. Furthermore, and to provide a base of comparison, it was acquired a set of results with no barrier.

Concerning the placement of the microphone and probe, their position was varied in a 2D plane as depicted in Figure 5. This variation had the goal of finding the optimal position for this assembly so that the vortex shedding frequency could be correctly detected. In z direction, according to Figure 5, the microphone was positioned at the distances $z = 2D$, $z = 3D$ and $z = 4D$. For each one of these z positions, the microphone was moved in the r direction from $r = 0$ until $r = R_{nozzle} + 3mm$, where R_{nozzle} is the radius of the convergent nozzle.

During these experimental tests, the room was kept, as much as possible, quiet and noiseless to ensure the quality of the results. Along with this, at the beginning of every set of tests, a background noise acquisition was done. In addition, an elec-

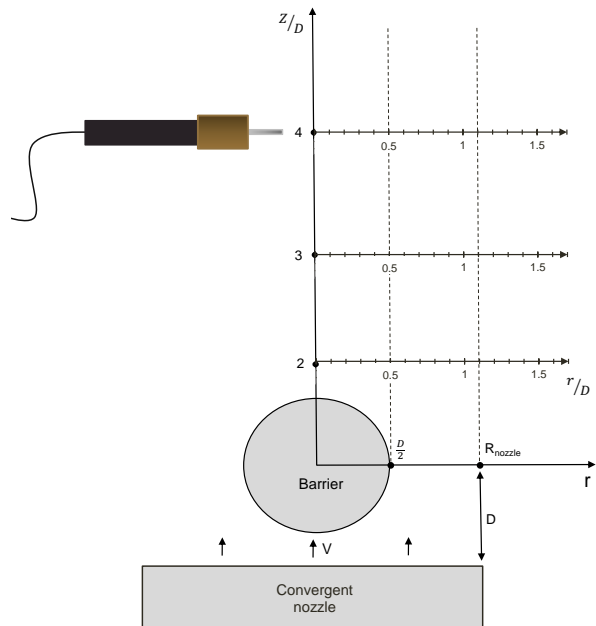


Fig. 5: Schematic view of the measurement system, for $D=5$ mm.

tronic noise acquisition was also performed.

3.3. Data Processing

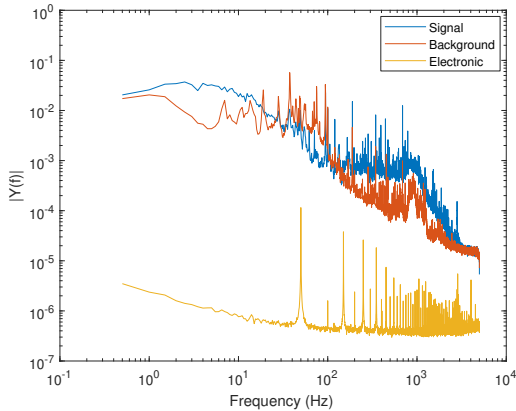
During the conducted experimental tests with the high speed imaging system, the previously defined air flow rate range was shortened to 1 - 5 SLPM. Past 5 SLPM, the flow is stronger and the aluminum oxide particles are very abundant, which can lead to damage of the camera lens. Another reason for this shortening is the lack of temporal resolution to capture the vortices for higher flow rates. In order to be able to have sufficient exposure, the exposure time had to be increased, resulting in a decrease in the number of fps. The majority of the films were recorded with 400 fps, which significantly reduces the temporal resolution.

After the recording, the films were analyzed in order to collect the most representative frames of the near and far wake. Small adjustments in the image contrast and brightness were made to provide better visualization.

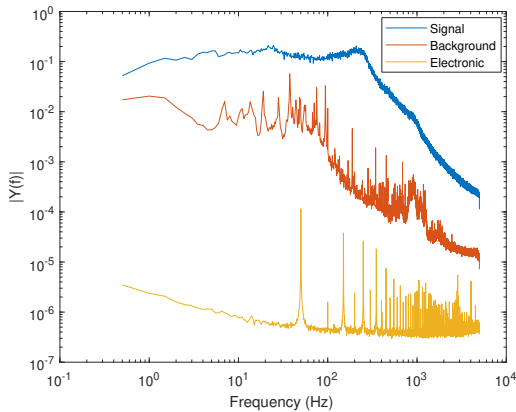
Regarding the pressure acquisition system, the signal processing performed is dependent on how the acquisition board acquires the data. As previously said, each round of acquisition performed is composed by $N = 50$ blocks of 20,000 points, resulting in a file of 1 million points. When analyzing this file, the application of the FFT algorithm is done separately for each one of these blocks, which leads to the obtainment of 50 different FFTs. After this, an ensemble averaged is performed, leading to the final result. This entire process has the goal of

reducing the random noise of the signal, producing better results [19]. The choice of $N = 50$ blocks was a trade-off between the reduction of random noise and the computational effort required.

After this, the quality of the obtained spectra was evaluated. For this, a plot despitng the FFT of the acquired signal, the background noise and electronic noise was done. The FFTs of the signal were analyzed for each imposed flow rate and for the same conditions, at the same point of the experimental setup with the same barrier.



(a) $Q=4$ SLPM and $V=0.70$ m/s.



(b) $Q=12$ SLPM and $V=2.10$ m/s.

Fig. 6: FFT of the signal, background noise and electronic noise. Frequency spectra obtained for $D=5$ mm, on the position $z/D = 2$ and $r/D = 0.9$.

Figure 6 shows the plot obtained for the minimum (4 SLPM) and maximum (12 SLPM) flow rates evaluated. Comparing these two plots, it can be observed that the amplitude of the signal obtained with 4 SLPM is similar to the amplitude of the background noise. For this reason, and to ensure the quality of the obtained results, the flow rates of 4 SLPM and 6 SLPM were not considered. Therefore, in Section 4, the results are only presented for 8 SLPM, 10 SLPM and 12 SLPM.

For the remaining flow rates, the vortex shedding frequency was obtained by analyzing the correspon-

dent frequency spectra. The procedure followed was to look for peaks in low-frequency ranges. For this, each spectrum was analyzed individually and the frequencies of the peaks were noted. In Figure 7, an example of an analyzed FFT is presented, along with the indication of two peaks. The peak (a) is not relevant for the scope of this study since it is found in the frequency of 1.5 Hz and is possibly caused by background noise. On the other hand, the peak (b), with a frequency of 136 Hz is possibly relevant.

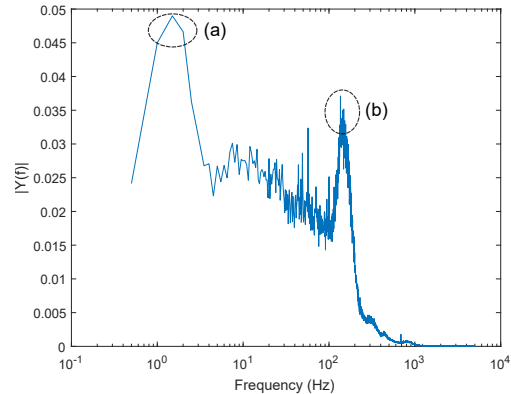


Fig. 7: Analyzed FFT with two highlighted peaks. Frequency spectrum obtained for $Q=8$ SLPM and $D=2$ mm, on the position $z/D = 4$ and $r/D = 2.5$.

When analyzing the frequency spectra obtained with the barrier of $D = 1$ mm, it was detected that this diameter was not adequate. This problem was discovered by comparing these results with the ones with no barrier and realizing that they did not present the vortex shedding frequency. A possible explanation for this lies in the dimension of the acoustic probe used, that has a tube with an inner of 3 mm, three times greater than the diameter of the barrier. Therefore, the results presented in in Section 4 will not consider the barrier with $D = 1$ mm.

4. Results

4.1. Visualization

The presented high speed imaging frames were chosen amongst the others to better illustrate the phenomenon of vortex shedding, namely the regions of the near and far wake. All the frames chosen have a resolution of 512×512 pixels.

Figure 8 shows the region close to the cylinder, the near wake, where it is possible to observe the recirculation area. This region is characterized by low velocities and constant pressure smaller than the surrounding area. The flow separation occurs at both right and left sides of the cylinder, which enables to see the difference between the velocities of the recirculation zone and the flow that passes around the cylinder, that moves at a higher veloc-

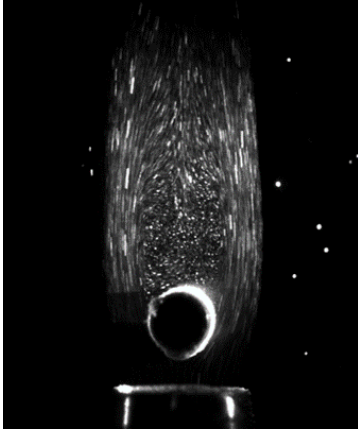


Fig. 8: High speed imaging frames of the near wake for $Re=177$. Image acquired at 400 fps and $2497 \mu s$.

ity. The vortex release is not noticeable, although according to the performed literature review is occurring for the analyzed Reynolds number. The problem can be the lack of temporal resolution to capture this event.

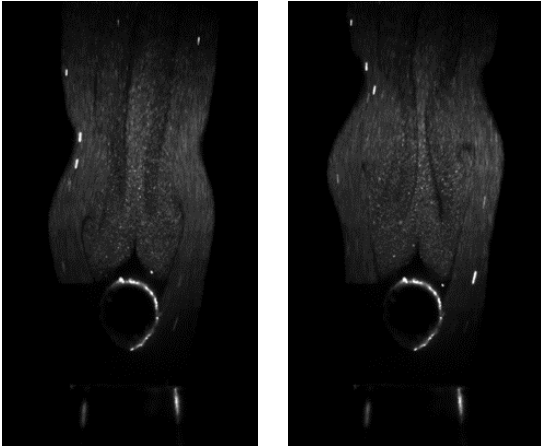


Fig. 9: High speed imaging frames of the near wake for $Re=118$. Acquired at 400 fps and $2497 \mu s$.

Figure 9 was captured for a smaller Reynolds number, $Re=118$. With this reduction, the vortex shedding frequency decreases, therefore requiring a smaller frame rate to capture its release. In these two frames, it is possible to see the vortex release that occurs firstly for the right side of the cylinder and then for the left one. The released vortices rotate in opposite directions and have symmetric strength. This instability in the near wake is what originates the vortex shedding effect that dominates the far wake.

Regarding the high speed recordings of the far wake, they were not as successful. These frames were taken at a higher frame rate, 1000 fps, and at a higher Reynolds number, $Re=234$. These parameters are different from the previous ones since

after an analysis they were the ones who provided for better visualization.

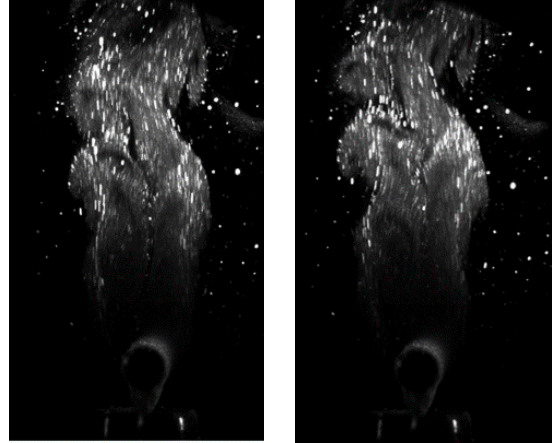


Fig. 10: High speed imaging frames of the far wake for $Re=234$. Acquired at 1000 fps and $997 \mu s$.

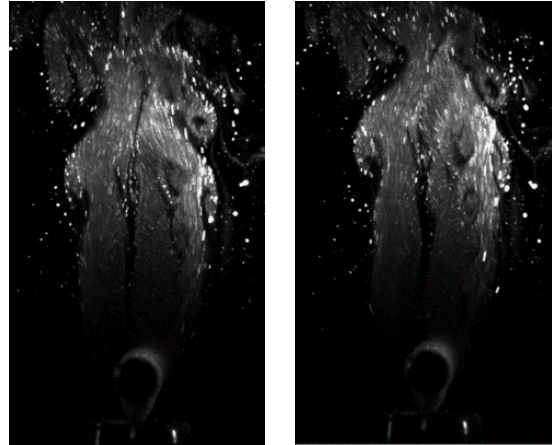


Fig. 11: Special attention to the formation of vortices shed from the right side of the cylinder. Same conditions as Figure 10.

Closely observing Figure 10, it is possible to see the twin vortices that were shed alternately from each side of the cylinder aligned along two parallel lines. A better visualization of the vortices is presented in Figure 11, where the ones originated from the right side of the cylinder are more noticeable. For the analyzed case, the detection of these type of vortices is hampered by the vortex formation of the free jet [20], that can also be observed in the frames. The fact that the cylinder diameter is nearly half of the convergent nozzle diameter ultimately mixes these two types of vortices, making it difficult to acquire good recordings of the vortex shedding.

To obtain a better visualization, the high speed imaging system should be optimized, mostly for providing better lighting. In this way, the frame rate of the high-speed camera does not have to be

so reduced, leading to a better temporal resolution. Another change that could be made is the increase in the difference between the convergent nozzle and the imposed barrier so that the free jet vortices are formed further away from the barrier, not creating interferences.

4.2. Vortex Shedding Frequency

The results acquired according to the measurement system presented in Figure 5 are displayed separately for the two analyzed barriers: $D=5$ mm and $D=2$ mm. For each case, the Reynolds number was calculated according to the equation:

$$Re = \frac{V D}{\nu_{air}}, \quad (3)$$

where the values of V are obtained from the Table 1.

The calculated Reynolds numbers vary between 189 and 707, being always higher for the diameter of 5 mm. According to the literature review, the vortex shedding effect occurs for $Re \geq 49$, so it should be possible to obtain the vortex shedding frequency for every case.

A. Barrier diameter: 5 mm

Figure 12 shows the selected peaks from the frequency spectra as a function of the radial and vertical distances to the center of the barrier, for a flow rate of $Q=12$ SLPM. The tendency of the results for the remaining flow rates is similar.

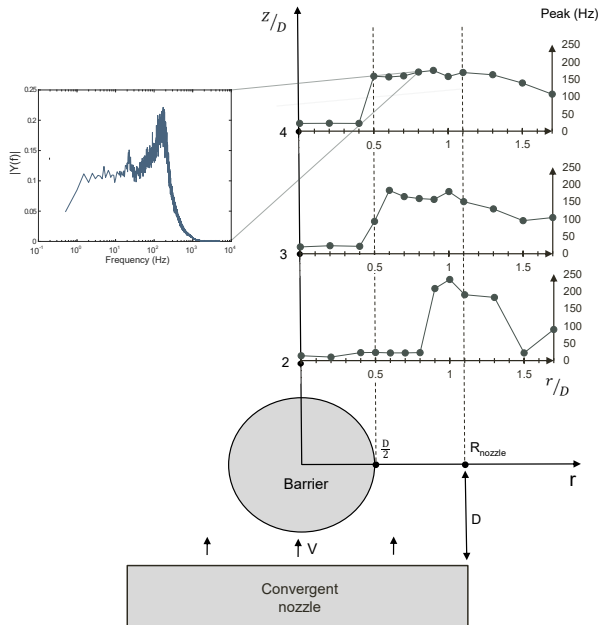


Fig. 12: Peaks of the FFTs obtained for $Q=12$ SLPM and $Re=707$, according to the radial and vertical distances to the center of the barrier.

In Figure 12, it is possible to see that the value of the frequency peak varies both according to

the radial and vertical distances to the barrier. At $z = 2D$, the acquired values are more variable, probably due to the proximity to the recirculation area. For $z = 3D$ and $z = 4D$, the values are increasingly lower and more stable.

Regarding the r axis, there is a tendency for higher values at $r = [D/2, R_{nozzle}]$. Besides this, for $r = [0, D/2[$, the values are close to zero, which was expected due to the location above the barrier.

It is possible to narrow down a more limited area of interest to detect the vortex shedding frequency, which corresponds to the area where the values are higher and more stable: $r = [D/2, R_{nozzle}]$ for $z/D = 3$ and $z/D = 4$. For these points, the acquired values were closely analyzed. In a first phase, the values were inspected separately for the two vertical distances $z/D = 3$ and $z/D = 4$. With this analysis, some outliers were detected, which corresponded to the position of $r = D/2$.

Following the removal of the outliers, the remaining results were analyzed simultaneously for the two vertical distances, resulting in Figure 13. Analyzing the values, it can be noticed that the measured frequency peak is similar between the two z positions. Also, there is a grouping around a certain bandwidth for each flow velocity.

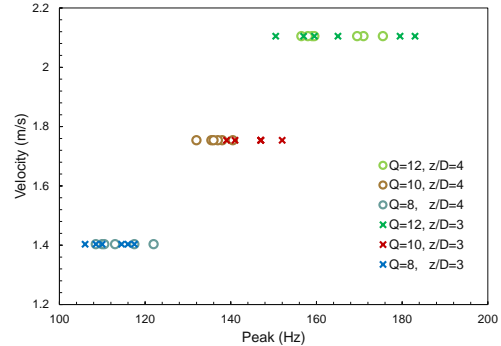


Fig. 13: Outlet velocity as a function of the frequency peak for $r =]D/2, R_{nozzle}]$ at $z/D = 3$ and $z/D = 4$. $D=5$ mm.

In order to make an estimation of the Strouhal number for this barrier, a more detailed analysis of the frequency peaks was done. With this, it was estimated a value of 0.4, which does not agree with the performed literature review that pointed to a value ~ 0.2 for the analyzed Reynolds numbers.

In an attempt to explain this result, an investigation related to free jet vortices was performed, due to its high interference presented in the recordings executed with the same barrier. It was found that for this type of vortices, a Strouhal number in the range of $0.31 \leq St \leq 0.61$ is obtained [20].

With this evidence, along with the one provided from the previously analyzed frames, it is possi-

ble to infer that the performed estimation of the Strouhal number had interference of free jet vortices. Therefore, a cylindrical barrier with a diameter of 5 mm is not adequate to obtain a measurement of the vortex shedding frequency and consequent usage in the proposed technique.

B. Barrier diameter: 2 mm

The results obtained for this diameter are presented similarly to the previous ones. Therefore, the scheme depicting the selected frequency peaks as a function of the vertical and radial distances is only presented for $Q=12$ SLPM.

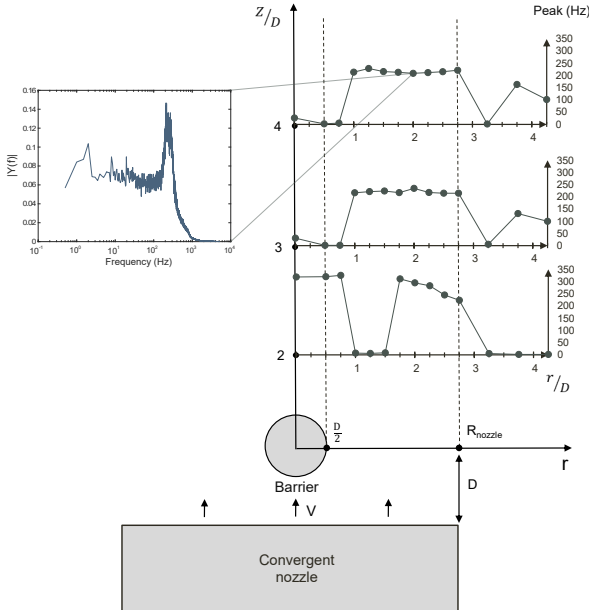


Fig. 14: Peaks of the FFTs obtained for $Q=12$ SLPM and $Re=283$, according to the radial and vertical distances to the center of the barrier.

In Figure 14, it is possible to see that also for this diameter the frequency peak varies according to the radial and vertical distances. In general, the same observations performed in Figure 12 remain valid.

Therefore, for the same reason, a limited area of interest was selected for $r = [D/2, R_{nozzle}]$ at the vertical distances of $z/D = 3$ and $z/D = 4$. Also for this case, there were found outliers that were traced to the radial positions of $r = D/2$ and $r = D/2 + 0.5$ mm, the two closest points to the barrier.

After rectifying the area of interest by removing the outliers, the remaining results were analyzed simultaneously for the two vertical distances, resulting in Figure 15. Analyzing these values, it can be noticed that the measured frequency peak is similar between the two vertical positions. Concerning each flow velocity, for $z/D = 3$ the measured values

are slightly higher than for $z/D = 4$.

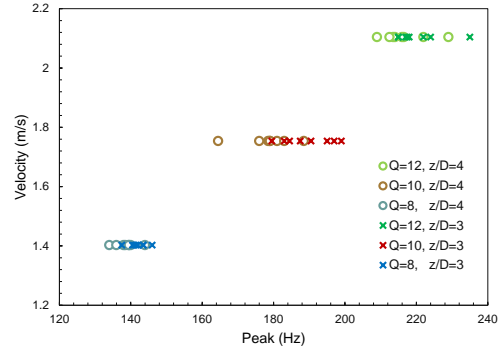


Fig. 15: Outlet velocity as a function of the frequency peak for $r = [D/2 + 1$ mm, $R_{nozzle}]$ at $z/D = 3$ and $z/D = 4$. $D=2$ mm.

To estimate the Strouhal number for this diameter, a detailed analysis of the frequency peak values was performed. In this analysis, it was obtained a value of 0.2 that is consistent with the literature. Therefore, it can be inferred that the measurements performed in the above-mentioned area of interest are capturing the vortex shedding frequency.

Accordingly, a cylinder-shaped barrier with a diameter of 2 mm is adequate to be a part of the proposed diagnostic technique. Nevertheless, since the performed experiments only evaluated two different diameters, it is possible that an equally or even better diameter exists.

In addition to the choice of the diameter, an equally important aspect is the position of the microphone that best measures the vortex shedding frequency. That position was already reduced to an area of interest. The goal is now to determine the best position.

The selected area of interest was: $r = [D/2 + 1$ mm, $R_{nozzle}]$ for $z/D = 3$ and $z/D = 4$. To be able to choose the best position, the amplitudes of the frequency peaks are evaluated.

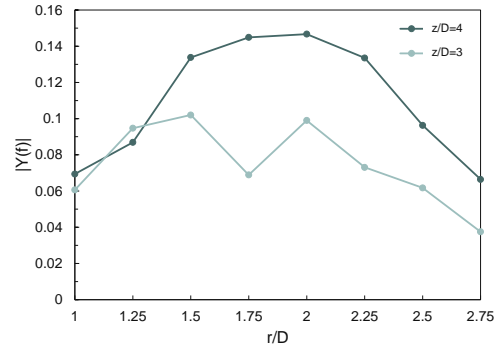


Fig. 16: Amplitude of the FFT for the selected peaks as a function of r/D , for $z/D = 3$ and $z/D = 4$. $Q=12$ SLPM.

In Figure 16, it is shown the amplitude of the frequency peak as a function of the radial distance of acquisition, for the flow rate of 12 SLPM. The tendency obtained for the remaining ones is similar, with smaller amplitudes corresponding to smaller flow rates.

In the majority of the positions, except for $r/D = 1.25$, the amplitude is significantly higher for the vertical distance of $z/D = 4$. With this analysis, it is possible to select the four more important points, all happening for $z/D = 4$: $r/D = \{1.5, 1.75, 2, 2.25\}$.

The frequency spectra of the four selected points (for each flow rate) was analyzed. This was done since a higher amplitude of the frequency peak does not necessarily mean an easier detection. It can be the case that the peak is not easily detectable due to other peaks with similar amplitude around it.

With the analysis of the frequency spectra, it was concluded that the more preminent peaks happen for $r/D = 2$ and $r/D = 2.25$, which are even higher than the background noise that appears for lower frequencies. For this reason, these are considered to be the best positions.

4.3. Analysis of the Proposed Technique

The previous sections aimed to determine a set of parameters that provide for the correct determination of the expiratory velocity using the vortex shedding frequency and the Strouhal number. As discussed, the parameters are:

Table 2: Determined parameters.

D (mm)	St	z/D	r/D
2	0.2	4	2 - 2.25

Additionally, the position of the barrier related to the convergent nozzle was set to D in all the performed experiments, since its change did not have impact on the results. Gathering these parameters, it is possible to design a scheme of the proposed technique, highlighting the distances of the barrier and microphone related to the nostril. This scheme is presented in Figure 17.

Once the goal of this technique is the determination of the nostril expiratory velocity, an estimation of the uncertainty of this value is important. The results obtained showed a relative error similar for the three tested cases that do not overcome $\sim 1.5\%$. Therefore, this method does not lose accuracy in the measurement of smaller velocities. This is important since the initial objective was to measure velocities around 1 m/s, that could still be accomplished once that the background noise limitations are withdrawn.

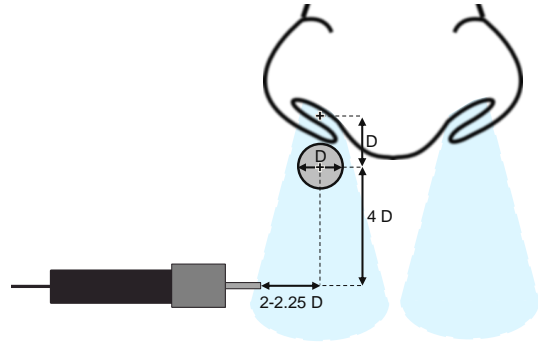


Fig. 17: Scheme of the proposed technique with the determined parameters.

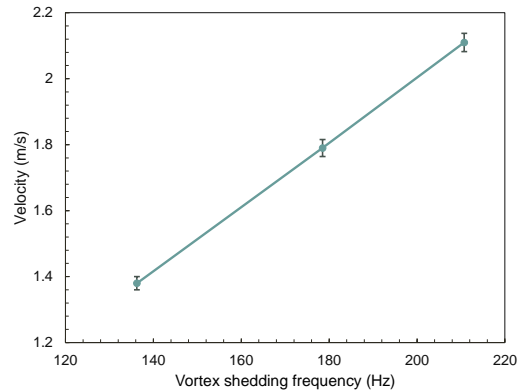


Fig. 18: Velocity of the expiratory flow as a function of the vortex shedding frequency, with vertical error bars.

Figure 18 shows the expiratory velocity as a function of the vortex shedding frequency with vertical error bars that correspond to the uncertainty of each velocity. It is expected that the expiratory velocities between the ones tested and the correspondent vortex shedding frequencies also follow a Strouhal number of 0.2. Furthermore, gathering the literature results and the ones obtained from this study, it is also predicted that for velocities higher than ~ 0.37 m/s ($Re \geq 49$) the expiratory velocity can be estimated with this method.

Nevertheless, in order to study the behavior for lower velocities, the peak detection system needs to be developed. The measurements must be done in an anechoic room or any other place that enables to reduce the background noise. With the experimental setup used to develop this thesis, only the vortex shedding frequency peaks for the strongest flow rate were detected above the background noise. Additionally, some filters with the objective of reducing the background noise can be applied.

5. Conclusions

The present work concluded by meeting the pre-established goals, although with some changes from

the initial plan. It introduced new findings in this field, with the presentation of a new technique and consequent determination of its operating parameters.

So that the determination of the previous parameters was possible, several simplifications were introduced when comparing with the real operation conditions. These simplifications were needed and are associated with the first development phase of the proposed diagnostic technique. More investigation needs to be performed to conclude this research and decide whether this is a reliable diagnostic technique or not.

References

- [1] R. K. Chandra, M. O. Patadia, and J. Raviv. Diagnosis of nasal airway obstruction. *Otolaryngologic Clinics of North America*, 42(2):207–225, 2009.
- [2] I. Serifoglu, I. I. Oz, M. Damar, M. C. Buyukuysal, A. Tosun, and Ö. Tokgöz. Relationship between the degree and direction of nasal septum deviation and nasal bone morphology. *Head & face medicine*, 13(1):3, 2017.
- [3] N. Fettman, T. Sanford, and R. Sindwani. Surgical management of the deviated septum: techniques in septoplasty. *Otolaryngologic Clinics of North America*, 42(2):241–252, 2009.
- [4] J. Yepes-Nunez, J. Bartra, R. Munoz-Cano, J. Sánchez-López, C. Serrano, J. Mullol, I. Alobid, J. Sastre, C. Picado, and A. Valero. Assessment of nasal obstruction: correlation between subjective and objective techniques. *Allergologia et immunopathologia*, 41(6):397–401, 2013.
- [5] D. W. Hsu and J. D. Suh. Anatomy and physiology of nasal obstruction. *Otolaryngologic Clinics of North America*, 2018.
- [6] N. Mygind and R. Dahl. Anatomy, physiology and function of the nasal cavities in health and disease. *Advanced drug delivery reviews*, 29(1-2):3–12, 1998.
- [7] A. Thomson and L. D. Buxton. Man’s nasal index in relation to certain climatic conditions. *Journal of the Anthropological Institute of Great Britain and Ireland*, pages 92–122, 1923.
- [8] D. Doorly, D. Taylor, and R. Schroter. Mechanics of airflow in the human nasal airways. *Respiratory physiology & neurobiology*, 163(1-3):100–110, 2008.
- [9] J. Keeler and S. P. Most. Measuring nasal obstruction. *Facial Plastic Surgery Clinics*, 24(3):315–322, 2016.
- [10] D. Lal and J. P. Corey. Acoustic rhinometry and its uses in rhinology and diagnosis of nasal obstruction. *Facial Plastic Surgery Clinics*, 12(4):397–405, 2004.
- [11] C. Bermüller, H. Kirsche, G. Rettinger, and H. Riechelmann. Diagnostic accuracy of peak nasal inspiratory flow and rhinomanometry in functional rhinosurgery. *The Laryngoscope*, 118(4):605–610, 2008.
- [12] O. Golubnitschaja. Paradigm change from curative to predictive medicine: Novel strategic trends in europe. *Croatian medical journal*, 50(6):596, 2009.
- [13] R. King. A review of vortex shedding research and its application. *Ocean Engineering*, 4(3):141–171, 1977.
- [14] B. T. Aydin. *Controlling the near-wake of a circular cylinder with a single, large-scale tripwire*. PhD thesis, 2014.
- [15] P. W. Bearman. Vortex shedding from oscillating bluff bodies. *Annual review of fluid mechanics*, 16(1):195–222, 1984.
- [16] S. Green. *Fluid vortices*, volume 30. Springer Science & Business Media, 2012.
- [17] A. d. O. C. Gomes, A. C. M. Sampaio-Teixeira, S. H. K. Trindade, and I. E. K. Trindade. Nasal cavity geometry of healthy adults assessed using acoustic rhinometry. *Brazilian journal of otorhinolaryngology*, 74(5):746–754, 2008.
- [18] I. Hahn, P. W. Scherer, and M. M. Mozell. Velocity profiles measured for airflow through a large-scale model of the human nasal cavity. *Journal of Applied Physiology*, 75(5):2273–2287, 1993.
- [19] H. Gustafsson, S. E. Nordholm, and I. Claesson. Spectral subtraction using reduced delay convolution and adaptive averaging. *IEEE Transactions on Speech and Audio Processing*, 9(8):799–807, 2001.
- [20] Y. Zaouali, T. Filali, H. B. Aissia, and J. Jay. Flow structure generated from an axisymmetric natural air jet at a moderate reynolds number. *Fluid Dynamics Research*, 43(3):035502, 2011.